Lattice models of polycrystalline microstructures: A quantitative approach

Antonio Rinaldi [a,b,*], Dusan Krajcinovic [b], Pedro Peralta [b], Ying-Cheng Lai [c]

[a] *Department of Chemical Science and Technology, University of Rome 'Tor Vergata', Via della Ricerca Scientifica, 00133 Roma, Italy*
[b] *Mechanical and Aerospace Engineering Department, Arizona State University, Tempe, AZ 85287-6106, United States*
[c] *Electrical Engineering, Arizona State University, Tempe, AZ 85287, United States*

Abstract

This paper addresses the issue of creating a lattice model suitable for design purposes and capable of quantitative estimates of the mechanical properties of a disordered microstructure. The lack of resemblance between idealized lattice models and real materials has limited these models to the realm of qualitative analysis. Two procedures based on the same methodology are presented in the two-dimensional case to achieve the rigorous mapping of the geometrical and the elastic properties of a disordered polycrystalline microstructure into a spring lattice. The theory is validated against finite elements models and literature data of NiAl. The statistical analysis of 900 models provided the effective Young's modulus and Poisson ratio as function of the lattice size. The lattice models that were created have in average the same Young's modulus of the real microstructure. However, the Poisson's ratio could not be matched in the two-dimensional case. The spring constants of the lattices from this technique follow a Gaussian distribution, which intrinsically reflects the mechanical and geometrical disorder of the microscale. The detailed knowledge of the microstructure and the Voronoi tessellation necessary to implement this technique are supplied by modern laboratory equipments and software. As an illustrative example of lattice application, damage simulations of several biaxial loading schemes are briefly reported to show the effectiveness of discrete models towards elastic anisotropy induced by damage and damage localization.
© 2007 Elsevier Ltd. All rights reserved.

1. Introduction

Discrete lattice models have been used over the past two decades for the study of heterogeneous materials. Hansen et al. (1989), Sahimi (2000), Krajcinovic and Basista (1991), Krajcinovic and Vujosevic (1998), Mastilovic and Krajcinovic (1999), Krajcinovic and Rinaldi (2005), Krajcinovic and Rinaldi (2005), Delaplace et al. (1996), He and Thorpe (1985) and others have shown that statistical lattice models offer a convenient framework for the study of the damage process associated to microcracks formation and growth. The usage of the statistics to account for the disorder of the microstructure is one distinctive feature of such statistical models. The representation of microstructure as a discrete structure rather than a continuum matrix is another characteristic.

Many engineering materials, such as metals or ceramics, have a polycrystalline heterogeneous

* Corresponding author. Tel.: +39 06 7259 4275; fax: +39 06 7259 4328.
E-mail address: Antonio.Rinaldi@uniroma2.it (A. Rinaldi).

structure made of grains with various crystallographic orientations, shapes, compositions and defects. Traditional continuum models of micromechanics adopt homogenization techniques to convert a disordered material into an equivalent continuum model on the macroscale. However, that approach is valid if the heterogeneous microstructure is statistically homogeneous, i.e. the effective properties of all "relevant random fields do not depend on position in space" (Kreher and Pompe, 1989). This assumption, reasonable in the pristine state, is not realistic in presence of cooperative phenomena between existing defects and/or microcracks. On the other side, discrete lattice models seem applicable also when the microstructure is not statistically homogeneous.

Lattice models have usually been used to gain only a qualitative understanding about the damage process. This was certainly the case for fuse lattices, percolation lattices or electrical networks in Hansen and Roux (2000) and Gouyet (1996). Also the mechanical networks referenced above are highly idealized models. A mechanical lattice model typically consists of sites, which represent grains, connected to nearest neighbors by either springs, trusses or beam elements. The position of the sites, their coordination number z and the properties of the elements, such as the stiffness and/or the strength, are regarded as random variables sampled from independent (and somewhat arbitrary) distributions, without reference to specific materials or real experimental data. The mechanical disorder is generally considered decoupled from morphological/geometrical disorder (Krajcinovic and Rinaldi, 2005), partially for the sake of simplicity and partially because more detailed information about the microstructure is required to establish a possible correlation.

Recent advances and spread of experimental techniques, such as "Orientation Imaging Microscopy" (OIM), started making detailed knowledge of microstructures economical and routinely available. OIM, which is a derivative of scanning electron microscopy (SEM), produces an approximate "picture" of a microstructure including (but not limited to) number of grains, geometry, mutual correlations, orientation of material axes (crystallography), second phases, defects, slip planes and cleavage planes. The increasing availability of experimental data at a detailed level raises the non-trivial problem of transferring the random properties of the microstructure to a lattice model. The procedures proposed by Monette and Anderson (1994), He and Thorpe (1985) and Garcia-Molina et al. (1988) are either based on mean-field theory or limited to isotropic materials, which are not easily applicable to disordered polycrystalline materials. Without a general discretization procedure to assign the lattice parameters, the wealth of high-quality experimental data is just a sterile prerequisite for the leap of lattice models from abstract mathematical schemes to practical engineering tool, capable of quantitative estimates.

This paper presents two procedures for constructing a spring network from "detailed knowledge" of the microstructure. The proposed methodology establishes the connection between the sampling distribution of spring stiffnesses and the morphology, geometry and mechanical properties of the microstructure. The results show that such distribution emerges naturally and does not need to be arbitrarily assigned a priori. Our discourse is limited to two-dimensional (2D) lattice models but the same ideas apply to the three-dimensional case. The ceramics NiAl is selected for the comparison between the literature data and the effective properties predicted from the models.

2. Scales and statistical models

The determination of material properties is scale-dependent and is related to the response of the material to applied stimuli and actions. Three scales are defined in this paper: the macroscale, the microscale and the grainscale.

The *macroscale* is the typical scale of engineering design and is the scale where the smallest observable element can be approximated as a continuum element, completely filled of homogeneous matter. The characteristic dimension of a specimen on the macroscopic level is denoted by L. At this level the microdefects are not observable and the material behavior is described in terms of effective properties which are representative of the underlying microstructure in an average sense. Macrocracks, notches, dents, perforations and shear bands among others belong to the class of defects observable on this scale. The stress–strain constitutive relations for a linear elastic solid are

$$\bar{\sigma}_{ij} = \bar{C}_{ijkl}\bar{\varepsilon}_{kl}, \tag{1}$$

where $\{\bar{\sigma}_{ij}, \bar{\varepsilon}_{kl}\}$ are the second-order tensors of the average stresses and average strains, respectively and $\bar{C}_{ijkl}$ is the fourth-order effective stiffness tensor with indices $i, j, k, l = 1..3$. The bar sign indicates that they are effective quantities.

The *microscale* is the scale where the random heterogeneous geometry of a unit volume of the material is observable (Krajcinovic, 1996). The characteristic length is the resolution length l with $l \ll L$. Details smaller than l are not captured by the model and a field at lower scale can be defined only by interpolation. Grain-boundaries, inclusions and voids are examples of microscale imperfections naturally present in the material. The size of the smallest grain-boundary is a convenient choice for l.

The *grainscale* is an auxiliary scale, properly selected and finer than the microscale, where "desired" properties of a grain are measurable. The choice of the resolution length of the grainscale l_G is problem dependent and $l_G \leqslant l$. The introduction of this scale is necessary when one is interested in some properties of phenomena related to a grain, such as single-crystal plasticity and inter-granular cleavage, and the selected microscale is not sharp enough. The size l_G could be chosen anywhere between the length of the lattice parameter of the underlying Bravais lattice (atomic scale) and the micro-resolution length l. In this paper it is assumed that $l \geqslant l_G \gg 1$ Å (Angstrom), i.e. the grain sizes are several orders of magnitude greater than the atomic scale to discard dislocations and quantum effects in the lattice model.

A microstructure is approximated on the microscale by the Delaunay triangular lattice, which is the topological dual representation of a Voronoi froth and is related to it by a Legendre transformation (Okabe et al., 1999; Zallen, 1983). The usage of approximate Voronoi froths in modeling the microstructure is becoming a common practice as proven by the many available commercial software packages that will fit a Voronoi tessellation to experimental data (in 2D or 3D obtained by serial sectioning), such as MIMICS, SURFDRIVER, AMIRA. Many papers are available where Voronoi tessellation are used to model real microstructures, such as Espinosa and Zavatteri (2003). Noticeably, while a Voronoi tessellation associated to a given clouds of Delaunay points is unique, there might be none or multiple Delaunay ensemble representative of one microstructure. For example, real grains are not regular polyhedrons (polygons in 2D) and do not always have convex shapes (concavities cannot be convex directly with the classic Voronoi construction made of convex tiles only). More advanced and complex tessellation techniques are available to overcome some of these issues. However, pursuing an exact representation of a real microstructure is not our intention here and might not be the best strategy either. Alternatively, it could be more fruitful to focus on the major statistics of a given microstructure (e.g. distributions of grain size and grain orientation, two-point or higher order correlation functions, etc.) to create Voronoi tessellations that are representative of such statistics. Different types of tessellations and their construction to achieve the "best" approximation represent an interest topic of future research.

By assuming that the Voronoi tessellation in Fig. 1 (full line) is a faithful reproduction of a real microstructure, the Delaunay network (dashed line) is the lattice model that we wish to characterize based on the geometrical and mechanical properties of the Voronoi polygons. The average size of the Voronoi polygons is the resolution length l of the microscale while the overall size of the lattice L corresponds to the macroscale. The link between any two nodes of the Delaunay lattice is a linear spring orthogonal to the dual grain-boundary representing the cohesive force between two adjacent grains. The springs are connected by hinges at the nodes, in a truss-like fashion, and no transversal load is applied along the span. In this scheme, external moments cannot be applied directly on the grains (nodes), which have just two translational degrees of freedom (DOF) in 2D. Beam elements, like for example in Schlangen and Van Mier (1991), could be used to transfer nodal moments at the cost of an extra rotational DOF for all the grains.

The DOF of the lattice are associated to the Delaunay points, which are fewer than the Voronoi points. Since the grains are reduced to point particles, the Delaunay lattice does not convey explicit information about the geometry but about the mechanical properties and the topology of the material on the microscale. As shown in Fig. 2, only the
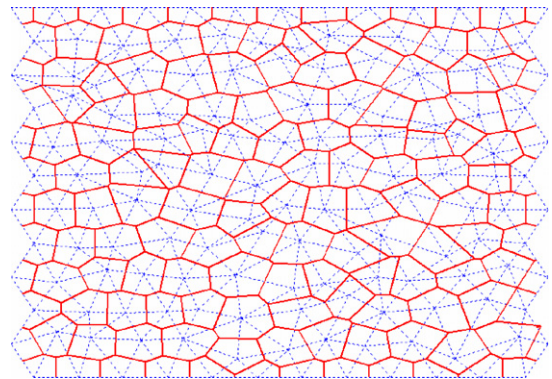

Fig. 1. Voronoi/Delaunay graphs of the microstructure.

macroscale and the microscale are defined in the lattice model. The grainscale is typical of the Voronoi representation, where each grain is a polygon and its area, geometry and number of sides (the grain-boundaries) are measurable. The Voronoi representation provides a crucial connection between the real microstructure and the lattice model. For the sake of comparison, a full finite element (FE) model of the microstructure based on the Voronoi tessellation is also analyzed here simultaneously to the lattice.

3. Creating a mechanically equivalent lattice

3.1. General idea: coupling the geometry and the mechanical properties

Figs. 2 and 3 depict the Voronoi polygon associated to a generic grain "O" with coordination number $z = 6$. Because the Voronoi edge is bisector of the corresponding Delaunay link, the six half-springs $\{OA^I, OB^I, OC^I, OD^I, OE^I, OF^I\}$ rest associated to grain O. It is postulated that each spring in the lattice is the series of two half-springs. From elementary mechanics the stiffness of any spring AB (Fig. 2) is

$$\frac{1}{K_{AB}} = \frac{1}{K_{AB'}} + \frac{1}{K_{BA'}} \qquad (2)$$

or $K_{AB} = K_{AB'}K_{BA'}/(K_{AB'} + K_{BA'})$. The problem of determining K_{AB} is now reduced to estimating the contributions of the grains A and B to the AB spring.

Polycrystalline materials are approximated as continuum media on the macroscale only in their pristine condition, but eventually the model breaks down when localization phenomena, such as damage localization, occur. However, if each single grain can be treated as a continuum solid, the techniques of linear elasticity are applicable on the grainscale. To our purposes the grainscale is large enough for the smallest grain to be modeled as a continuum homogeneous linear elastic solid. The mechanical properties of the crystal are described by the fourth-order stiffness tensor C^M_{ijkl} ($i, j, k, l = 1..3$) or by the 6×6 stiffness matrix $\mathbf{C_M}$ in Voigt's notation (Appendix A). A series of further assumptions is made in the remainder of the paper:

1. the grain is a linear homogeneous 2D elastic solid and deformations are small;
2. the stiffness matrix $\mathbf{C_M}$ and the orientation of the material axes are known for all grains;
3. the material symmetry groups satisfy the conditions for 2D problems; i.e. the components of $\mathbf{C_M}$ comply with the requirement provided in Ting (1996) for plane strain and plane stress problems of anisotropic solids:

$$C_{14} = C_{15} = C_{24} = C_{25} = C_{46} = C_{56} = 0 \qquad (3)$$

4. the grains are convex polygons;
5. the grain is partitioned in z counter-clockwise oriented triangles $\{O12, O23, O34, O45, O56, O61\}$ as shown in Fig. 3.

Without loss of generality and in compliance with Assumption 3, the more restrictive case of
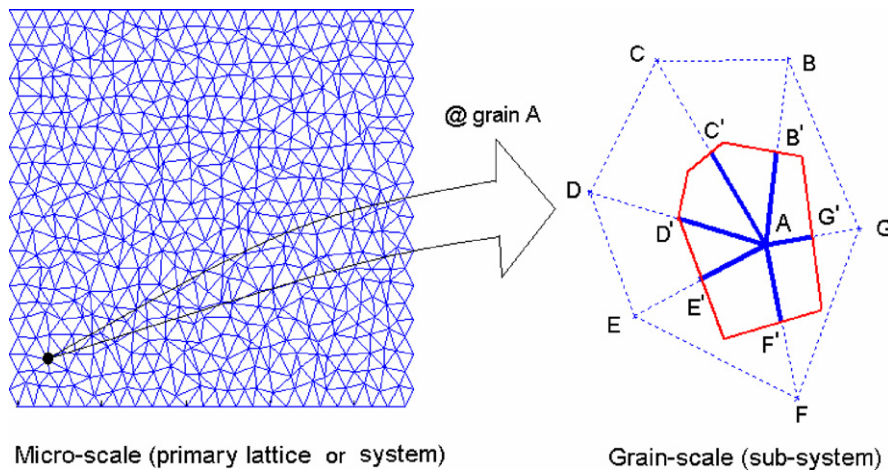

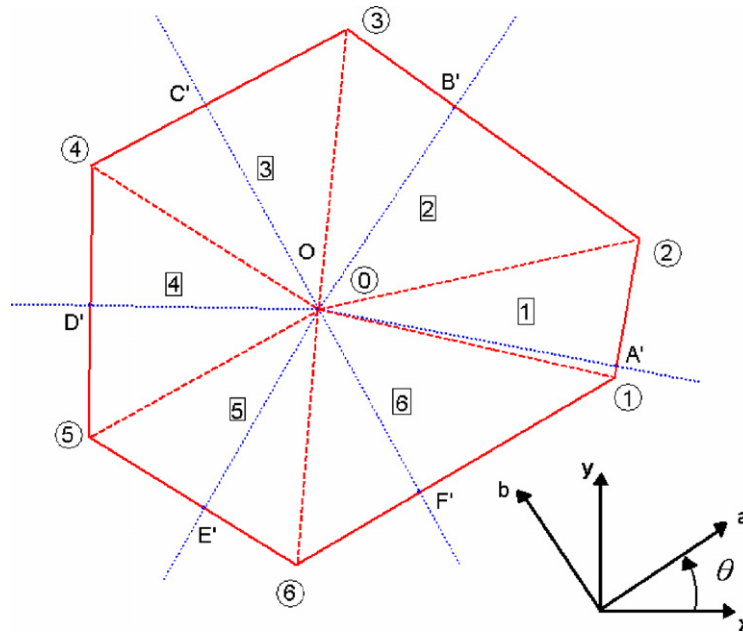Fig. 2. Microscale and grainscale. The points $\{A, B, C, D, E, F, G\}$ are global DOF of the lattice whereas the set $\{B', C', D', E', F', G'\}$ that marks the midpoints of the springs is observable on the smaller scale but hidden on the microscale.

Fig. 3. Partition of the Voronoi polygon associated to grain "O" with $z = 6$ into triangular elements (CST). The material axes are at θ degrees from the global frame of reference. The grain-elements has 7 nodes and is made of the 6 triangular elements.

orthotropic materials, with $\mathbf{C}_M$ expressed in the local frame of reference a–b–c, is considered for simplicity. Orthotropic materials require the specification of nine elastic constants and encompass rhombic, orthorhombic, cubic, and isotropic materials as special cases. Many engineering ceramics, such as MgO, NiAl and Ni_3Al have cubic symmetry and are specified by three elastic constants only. For the 2D case $\mathbf{C}_M$ is a 4×4 matrix and is conveniently expressed in the material axes a–b–c, where c is the out of plane axis (Jones, 1975). The representation of the stiffness matrix $\mathbf{C}_M^G$ in global x–y coordinates is obtained from the matrix transformation:

$$\mathbf{C}_M^G = \mathbf{Q}(\theta)\mathbf{C}_M\mathbf{Q}^T(\theta), \tag{4}$$

where $\mathbf{Q}(\theta)$ is a 4×4 matrix and depends only on the orientation of the material axes a–b around c (Appendix A). With this premise, two procedures are presented next. In the first one, named Lattice 1 (L1), the spring stiffnesses are computed from ordinary triangular finite elements. In the second one, named Lattice 2 (L2), the concept of "grain element" is exploited.

3.2. Procedure L1: using the triangular elements

By assigning proper BCs at the grain-boundaries, a well-posed elastic problem can be formulated in a variational form for each grain. The potential energy of an elastic grain of volume V_G is defined as

$$\Pi = U - W, \tag{5}$$

where

$$U = \int_{V_G} \boldsymbol{\varepsilon}^T[\hat{\mathbf{C}}_M^G\boldsymbol{\varepsilon}]\mathrm{d}V \tag{6}$$

is the strain energy and

$$W = \int_{V_G} \mathbf{b} \cdot \mathbf{u}\,\mathrm{d}V + \int_{\partial V_G} \hat{\mathbf{s}} \cdot \mathbf{u}\,\mathrm{d}a \tag{7}$$

is the "work potential" associated with the body forces $\mathbf{b}$ and the boundary tractions $\hat{\mathbf{s}}$. The unknown displacement field $\mathbf{u}$ is found from the "principle of minimum potential energy" by minimizing the potential energy Π (Gurtin, 1975). In (6) $\boldsymbol{\varepsilon} = [\varepsilon_{xx}, \varepsilon_{yy}, \gamma_{xy}]^T$ is the 3×1 strain vector and $\hat{\mathbf{C}}_M^G$ is a 3×3 reduced stiffness matrix derived from the 4×4 matrix $\mathbf{C}_M^G$ in (4). $\hat{\mathbf{C}}_M^G$ depends on the problem type and for the plane stress case, it is

$$\hat{\mathbf{C}}_M^G = \begin{vmatrix} c_{11}^{M,G} - \frac{(c_{13}^{M,G})^2}{c_{33}^{M,G}} & c_{12}^{M,G} - \frac{c_{13}^{M,G}c_{23}^{M,G}}{c_{33}^{M,G}} & 0 \\ & c_{22}^{M,G} - \frac{(c_{23}^{M,G})^2}{c_{33}^{M,G}} & 0 \\ symm & & c_{44}^{M,G} \end{vmatrix}, \tag{8}$$

while for the plane strain problem it is

$$\hat{\mathbf{C}}_{M}^{G} = \begin{vmatrix} c_{11}^{M,G} & c_{12}^{M,G} & 0 \\ & c_{22}^{M,G} & 0 \\ symm & & c_{44}^{M,G} \end{vmatrix}. \tag{9}$$

An approximate "kinematically admissible" displacement field (satisfying the essential BCs on the displacement) can be obtained via the finite element method (FE) in the isoparametric formulation (Fung and Tong, 2001). The above mentioned z adjacent triangles of Fig. 3 provide an intrinsic mesh for the grain and are labeled like $\boxed{i}$. The approximate strain vector for each element is

$$\hat{\boldsymbol{\varepsilon}} = \mathbf{B}\mathbf{d}_e, \tag{10}$$

where $\mathbf{B}(x, y)$ is a matrix of polynomials dependent on the choice of the shape functions and $\mathbf{d}_e$ is the element vector of unknown nodal displacements. The size of $\mathbf{B}$ and $\mathbf{d}_e$ are $3 \times 2p$ and $2p \times 1$ respectively, with "p" being the number of nodes in the triangle. For simplicity, linear shape functions are used in this study, i.e. the triangles are C^0-linear triangular elements with $p = 3$, better known as constant strain triangle (CST) (Fung and Tong, 2001). The z Voronoi points and the Delaunay center point are the FE nodes associated to the grain with the labeling scheme in Fig. 3 (circled labels). With such discretized model of the grain has $2(z + 1)$ degrees of freedom and the "approximate" strain energy function upon substituting $\boldsymbol{\varepsilon}$ with $\hat{\boldsymbol{\varepsilon}}$ becomes

$$U = \sum_{i=1}^{z} \left[\frac{1}{2} \mathbf{d}_e^T \mathbf{K}_e \mathbf{d}_e \right]_i = \frac{1}{2} \mathbf{d}^T \mathbf{K}_{GE} \mathbf{d} \tag{11}$$

with the subscript "e" indicating quantities defined at the element level as opposed to the system level. The sum over the z CST elements refers to the assembly procedure, with each $\mathbf{K}_e$ augmented to

$2(z + 1) \times 2(z + 1)$ before summing. The vector $\mathbf{d}_e = [u_0, v_0, u_1, v_1, u_2, v_2]^T$ is the 6×1 element vector of nodal displacements, $\mathbf{K}_e$ is the 6×6 element stiffness matrix and $\mathbf{d} = [u_0, v_0, u_1, v_1..u_z, v_z]^T$ is the $2(z + 1)$ system vector of nodal displacements of the selected grain. $\mathbf{K}_{GE}$ is the $2(z + 1) \times 2(z + 1)$ system (grain) stiffness matrix after the assembly. The element stiffness matrix $\mathbf{K}_e$ of each element is computed from

$$\mathbf{K}_e = \int_{V_G} \mathbf{B}^T \hat{\mathbf{C}}_M^G \mathbf{B} \, dV, \tag{12}$$

which in general requires numerical integration. For the CST triangular elements $\mathbf{B}$ is a 3×6 constant matrix and $\mathbf{K}_e = tA\mathbf{B}^T\hat{\mathbf{C}}_M^G\mathbf{B}$, with t being the thickness of the grain (taken as unit here) and A the area of the triangle. The assumption of counter-clockwise orientation of the z triangles $\{O12, O23, O34, O45, O56, O61\}$ guarantees that $\mathbf{K}_e$ is positive definite (with proper applied boundary conditions) and that the A is a positive area. The Voronoi points are arranged into a topological database of CSTs where the vertices O–A–B of the triangle OAB satisfy $(OA \times OB) \cdot \vec{z} > 0$.

The stiffness of the half-springs $\{OA^I, OB^I, OC^I, OD^I, OE^I, OF^I\}$ can be estimated from the stiffness matrix $\mathbf{K}_e$ of the corresponding CST elements $\{O12, O23, O34, O45, O56, O61\}$ in Fig. 3. If a unit displacement is imparted along OA to nodes 1 and 2 of the CST in Fig. 4 while node O is fixed, one can solve

$$\mathbf{F}_e = \mathbf{K}_e \mathbf{d}_e, \tag{13}$$

where $\mathbf{F}_e$ is the vector of the nodal forces of the CST. As the displacements of all 3 nodes are assigned, Eq. (13) is simply
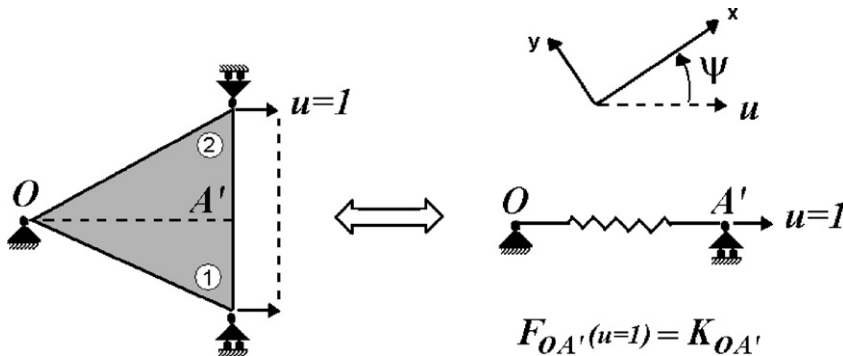

Fig. 4. Equivalence between CST and corresponding half-spring.

$$
\begin{vmatrix} F_x^0 \\ F_y^0 \\ F_x^1 \\ F_y^1 \\ F_x^2 \\ F_y^2 \end{vmatrix} = \mathbf{K}_e \begin{vmatrix} 0 \\ 0 \\ \cos(\psi) \\ \sin(\psi) \\ \cos(\psi) \\ \sin(\psi) \end{vmatrix}, \tag{14}
$$

where all elements in $\mathbf{F}_e$ are unknown. Consequently, $F_{ex}^0 = (k_{13}^e + k_{15}^e)\cos(\psi) + (k_{14}^e + k_{16}^e)\sin(\psi)$ and $F_{ey}^0 = (k_{23}^e + k_{25}^e)\cos(\psi) + (k_{24}^e + k_{26}^e)\sin(\psi)$. By imposing the "equivalence of force components" at node O between the CST and the half-spring under unit axial virtual displacement, the component along OA of the reaction in O, $\mathbf{F}_e^0$, equals the axial force $\mathbf{F}_{OA}$ in the half-spring OA^I, which for the unit elongation equals numerically the stiffness of the half-spring K_{OA}

$$
F_{OA}(\Delta\lambda = 1) = \mathbf{F}_e^0 \cdot \frac{OA}{|OA|} = K_{OA} \tag{15}
$$

with $\Delta\lambda$ being the elongation of the half-spring. It can be shown that (15) is well-posed because it satisfies the equivalence of the strain energy between the CST and the half-spring for the given deformation (Appendix B). Given $\mathbf{C}_M$ and the orientation of the material axes for all grains, the calculations can be repeated for all CST to compute the stiffness of all the springs in the lattice via Eqs. (2) and (15).

3.3. Refined procedure L2: using the grain element

The concepts of the previous section can be developed from a different point of view to derive an alternative procedure. In (12), $\mathbf{K}_{GE}$ is the $2(z + 1) \times 2(z + 1)$ stiffness matrix of the system (where the system consists of the linear elastic grain in Fig. 3). $\mathbf{K}_{GE}$ can be interpreted as the element stiffness matrix of the "grain element" (GE) defined by the $z + 1$ nodes $\{O, 1, 2, 3, 4, 5, 6\}$. The computation of $\mathbf{K}_{GE}$ is easily done by assembling the 6×6 stiffness matrices, $\mathbf{K}_e^{(p)}$ $(p = 1..z)$, of the z CST elements (Fung and Tong, 2001). According to the labels in Fig. 3, if O is taken as node 0 and is listed as first node for all triangles, the displacement vector of the GE is $\mathbf{d} = [u_0, v_0, u_1, v_1, u_2, v_2, u_3, v_3, u_4, v_4, u_5, v_5, u_6, v_6]^T$ and the stiffness matrix $\mathbf{K}_{GE}$ has the following structure

$$
\mathbf{K}_{\mathrm{GE}\,(14\times14)} = \begin{vmatrix}
x & x & x & x & x & x & x & x & x & x & x & x & x & x \\
 & x & x & x & x & x & x & x & x & x & x & x & x & x \\
 & & x & x & x & x & 0 & 0 & 0 & 0 & 0 & 0 & x & x \\
 & & & x & x & x & 0 & 0 & 0 & 0 & 0 & 0 & x & x \\
 & & & & x & x & x & x & 0 & 0 & 0 & 0 & 0 & 0 \\
 & & & & & x & x & x & 0 & 0 & 0 & 0 & 0 & 0 \\
 & & & & & & x & x & x & x & 0 & 0 & 0 & 0 \\
 & & & & & & & x & x & x & 0 & 0 & 0 & 0 \\
 & & & & & & & & x & x & x & x & 0 & 0 \\
 & & & & & & & & & x & x & x & 0 & 0 \\
 & & & & & & & & & & x & x & x & x \\
 & & & & & & & & & & & x & x & x \\
 & & & & & & & & & & & & x & x \\
symm & & & & & & & & & & & & & x
\end{vmatrix}
\begin{matrix} u_0 \\ v_0 \\ u_1 \\ v_1 \\ u_2 \\ v_2 \\ u_3 \\ v_3 \\ u_4 \\ v_4 \\ u_5 \\ v_5 \\ u_6 \\ v_6 \end{matrix},
$$

where "x" is a placeholder for non-zero terms. As an important remark, the GE does not have its own shape functions and the displacement field is interpolated from the nodal displacements in a piecewise fashion from the set of shape functions of the CST in each of the z regions. The main advantages of this construction are:

1. no need to formulate a new set of z shape functions and no need to identify a "parent element" with un-distorted shape and variable number of sides to carry out the Gaussian integration of Eq. (12) (Fung and Tong, 2001);
2. usage of higher-order triangular elements (quadratic or higher order) to obtain continuity of the strain field and increase the accuracy over the grain domain;
3. the formulation is not limited to convex polygon and concavities can be dealt with by redefining the CSTs partition.

The Voronoi tessellation is an intrinsic mesh of the polycrystalline microstructure and each grain is an element. The GE renders this option straightforward at the same computational cost of a random mesh containing an equal number of CST elements. The FE model has many more DOF and requires much more memory for both storage and calculations. Anyway, the FE option becomes very attractive when only a non-Voronoi tessellation of the microstructure is available.[1] In this case there is no Delaunay lattice but the GE can still be defined by selecting an inner point for each grain. The choice could be arbitrary or based on some

---

[1] Experimental measures from OIM for example do not routinely produce a Voronoi tessellation.

optimization criterion, like the minimization of the distortion of the CSTs elements of the grain.

For our purposes, the GE is be used to obtain a second different estimate for the stiffness of the springs in the Delaunay network. Eq. (15) discards the fact that the edges O1 and O2 of triangle ① in Fig. 3 are shared by the adjacent triangles ② and ⑥ and, hence, are constrained and not free. To account for such continuity, we can solve $\mathbf{F}_{GE} = \mathbf{K}_{GE}\mathbf{d}_{GE}$ rather than $\mathbf{F}_e = \mathbf{K}_e\mathbf{d}_e$ when a unit virtual displacement is applied along OA to nodes 1 and 2 while all the other nodes of the GE are locked in place. The reaction in O, $\mathbf{F}_{GE}^0$, differs from $\mathbf{F}_e^0$ and

$$F_{OA}(\Delta\lambda = 1) = \mathbf{F}_{GE}^0 \cdot \frac{OA}{|OA|} = K_{OA} \qquad (16)$$

provides a new estimate for K_{OA} in alternative to the one from (15). Fig. 5 pictures the two scenarios.

3.4. Considerations

The Voronoi tessellation is very important for the procedures L1 and L2. Relevant and non-trivial issues such as the existence or the construction of the best Voronoi approximation of a microstructure from experimental measures are not examined in this paper.

The lattice L1 is more compliant than the lattice L2 due to the increasing degree of constraint of the triangular elements in the GE. Furthermore, the lattice per se is expected to be more compliant than the real microstructure or than the corresponding FE model formed by CST elements. The cause resides in the ''solidity'' of the grain, which is lost in the selected discrete model where the springs are connected by hinges at the end-nodes and do not inter-

act transversely. The usage of beam elements or the addition of transversal springs could provide an effective way to approach this problem. In order to obtain a lattice with comparable effective properties, the estimates of the stiffness from (2) and either (15) or (16) must be corrected.

In the study of inelastic processes the springs are not perfectly linear and more sophisticated micro-constitutive relations are required. In damage mechanics, for example, a finite tensile strength is randomly assigned to each spring so that a rupture occurs when the load in the spring reaches the given threshold (Mastilovic and Krajcinovic, 1999; Krajcinovic and Rinaldi, 2005). Unlike the spring stiffness distribution though, the strength distribution is strongly dependent on the manufacturing process and the presence of non-visible defects ($<l$), such as glassy pockets, voids and second phase precipitates at the grain-boundary, renders any estimate of critical strains from pure geometrical considerations unreliable. This paper deals solely with the calibration of the stiffness distribution, while the selection of any other auxiliary distributions necessary to quench disorder in discrete statistical models constitute a topic for future research.

4. Lattice refinement

4.1. Test strategy

A series of test cases is designed to assess the properties of the lattices L1 and L2. Experimental data from the NiAl intermetallic are used to calibrate the parameters of a lattice that has same number of grains N on each side in a variety of situations. Tensile tests in both plane stress and
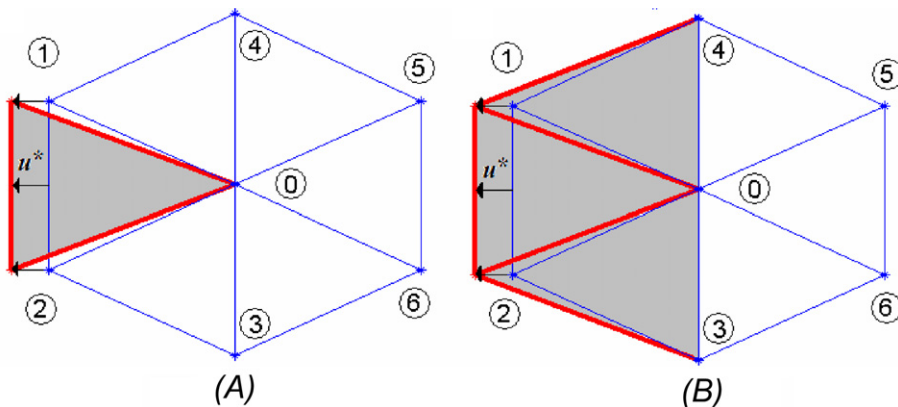

Fig. 5. Comparison of procedure L1 (A) and L2 (B) for a generic virtual displacement u^* applied to nodes 1 and 2.

plane strain conditions are simulated to measure the effective Young's modulus E_{eff} and Poisson's ratio v_{eff} (Fig. 6). The lattice results are compared against the associated FE model (FEA) made of GE elements.

The grain-boundaries of NiAl and other ceramics vary in a wide range but a linear length of $\approx 100 \ \mu m$ is a reasonable average (Davidge, 1979) and can be chosen as the resolution length of the lattice. A perfect triangular lattice is considered for simplicity as shown in Fig. 6. The material axes are assigned randomly to each grain by sampling the angle θ between the material axis a and the global x–y axes from a uniform distribution in $[0, \pi]$ (Fig. 3). Four lattice sizes $N = [12, 24, 48, 96]$ were compared to assess the convergence of the effective parameters. A sparse direct solver was employed for both spring network and the FEA model because of the "sparsity" (the ratio of the non-zero entries over the total number of elements in a matrix) of the global stiffness matrix of the polycrystalline microstructure. Table 1 reports number of grains, elements, DOF and sparsity for the considered lattice sizes. The full FEA model requires about three times as many

Fig. 6. Microstructure geometry and loading configuration used for the tests.

degrees of freedom as the lattice for any given size N.

Three choices of $\mathbf{C_M}$ were analyzed separately. NiAl is a brittle ceramics at room temperature and the single crystal has a cubic symmetry in the material frame of reference formed by the axes $a = [1, 0, 0]$ $b = [0, 1, 0]$ and $c = [0, 0, 1]$. From literature (Miracle, 1993) the 4 by 4 stiffness matrix $\mathbf{C_M^{001}}$ corresponding to such orientation is

$$\mathbf{C_M^{001}} = \begin{vmatrix} 200 & 133 & 133 & 0 \\ & 200 & 133 & 0 \\ & & 200 & 0 \\ symm & & & 114 \end{vmatrix}_{4\times 4} \text{GPa}, \quad (17)$$

which satisfies condition (3) for the 2D problem and so does the transformed matrix $\mathbf{C_M^G}$ from (4) for any rotation θ around the c-axis. Another compatible material frame of reference selected for our simulations corresponds to the axes $a = [-1, 1, 0]$, $b = [0, 0, 1]$ and $c = [1, 1, 0]$, where NiAl has orthotropic symmetry. The associated stiffness matrix $\mathbf{C_M^{110}}$ is

$$\mathbf{C_M^{110}} = \begin{vmatrix} 281 & 133 & 52 & 0 \\ & 200 & 133 & 0 \\ & & 281 & 0 \\ symm & & & 114 \end{vmatrix}_{4\times 4} \text{GPa}, \quad (18)$$

which has a lower symmetry than (17) but yet satisfies Eq. (3) for any arbitrary rotation around the $[1, 1, 0]$ axis. The choice of testing two different $\mathbf{C_M}$ matrices is not casual but is dictated by statistical considerations. Since the grains have same $\mathbf{C_M}$ and same global z-axis (c-axis) but different $\mathbf{C_M^G}$, the macroscopic properties E_{eff} and v_{eff} of polycrystalline NiAl deduced from the tensile test reflect the average on the microscale of the mechanical properties in the x–y plane. The matrices $\mathbf{C_M^G}$ sampled on the $\{0, 0, 1\}$ plane and the ones sampled on the $\{1, 1, 0\}$ plane form two different ensembles with different E_{eff} and v_{eff}. A meaningful perspective about
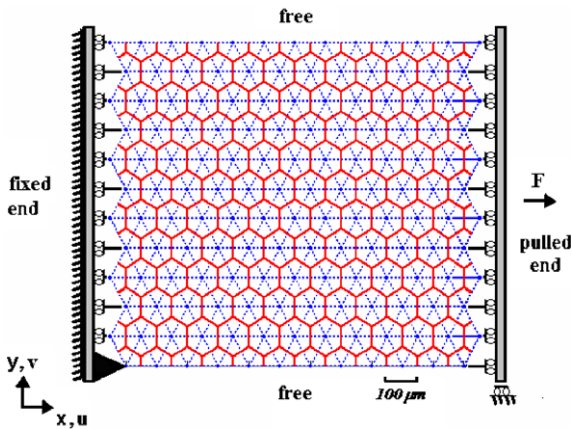
Table 1
Prospect of model information and number of tests

N	Sample size	Grains	Links	DOF		Sparsity (%)		Cases	Tot tests
				FEA	Lattice	FEA	Lattice		
12	15	150	402	896	300	1.37	3.32	5	75×3
24	15	588	1668	3524	1176	0.36	0.89	5	75×3
48	15	2328	6792	13,964	4656	0.09	0.23	5	75×3
96	15	9264	27,408	55,580	18,528	0.023	0.058	5	75×3
									$300 \times 3 = 900$

the sampling space is gained by examining the equivalent Young's modulus $E^* = 1/\mathbf{S}_{11}^G$, where $\mathbf{S}^G$ is the global compliance matrix of the grain and inverse of the selected $\hat{\mathbf{C}}_M^G$ from either (8) or (9). The sampling space is multi-dimensional because all the in-plane components of $\mathbf{C}_M^G$ influence E_{eff} and v_{eff}. Nevertheless, E^* is highly correlated to the stiffness of the grain in the test direction, which is the most influential on E_{eff}. The function $E^*(\theta)$ reveals what orientations offer greater stiffness and what the approximate shape of the sampling space is. Figs. 7 and 8 show, both in polar and Cartesian representations, the comparison between the sampling spaces associated to the $\{0,0,1\}$ and $\{1,1,0\}$ planes for plane stress and plane strain cases, respectively. The values of E^* are consistently higher on the $\{1,1,0\}$ plane of NiAl crystal, which leads to the expectation of higher vales of E_{eff} and v_{eff} when using (18) for $\mathbf{C}_M$. This invites to caution in comparing experimental data with numerical data from 2D models. Only a 3D model allows a full random sampling of $\mathbf{C}_M^G$, while 2D models always provide estimates of the parameters within a subspace.

A third and last choice for $\mathbf{C}_M$ consisted of an ideal isotropic single crystal that was deliberately "created" from (17) by setting $\mathbf{C}_M^{66} = E/2(1-v)$, i.e.

$$\mathbf{C}_M^{ISO} = \begin{vmatrix} 200 & 133 & 133 & 0 \\ & 200 & 133 & 0 \\ & & 200 & 0 \\ symm & & & 33.7 \end{vmatrix}_{4\times 4} \text{GPa} \qquad (19)$$

with $E = 94.3$ GPa and $v = 0.399$ computed as in (A.6). The isotropic case offers an interesting benchmark because a well-known mapping exists between

an isotropic continuum solid and a perfect triangular lattice (Monette and Anderson, 1994). The estimates of E_{eff} and v_{eff} are expected to match the values of the single crystal due to the complete symmetry of (19) (rotational invariance). In summary, five test cases are analyzed:

1. NiAl[0 0 1]: $\mathbf{C}_M^{001}$ from (19) and $\hat{\mathbf{C}}_M^G$ in plane stress from (8);
2. NiAl[0 0 1]: $\mathbf{C}_M^{001}$ in (19) and $\hat{\mathbf{C}}_M^G$ in plane strain from (9);
3. NiAl[1 1 0]: $\mathbf{C}_M^{110}$ from (20) and $\hat{\mathbf{C}}_M^G$ in plane stress from (8);
4. NiAl[1 1 0]: $\mathbf{C}_M^{110}$ from (20) and $\hat{\mathbf{C}}_M^G$ in plane strain from (9);
5. NiAl[ISO]: $\mathbf{C}_M^{ISO}$ from (19) and $\hat{\mathbf{C}}_M^G$ in plane stress from (8).

The mean estimates $\langle E_{eff}\rangle$ and $\langle v_{eff}\rangle$ in each case are obtained by averaging E_{eff} and v_{eff} over a statistical sample of 15 random microstructures for each size N. All replicates in the sample have same geometry but differ in the distribution of material axes. As shown in Table 1, one finite element model (FEA) and two lattices (L1 and L2) were created for the five test cases and for each microstructure (for a total of 900 models).

4.2. Test results

The statistical results of the simulations are summarized in Tables 2 and 3 (raw data not reported). The former table contains the mean values $\langle E_{eff}\rangle$ and $\langle v_{eff}\rangle$ while the latter contains the standard
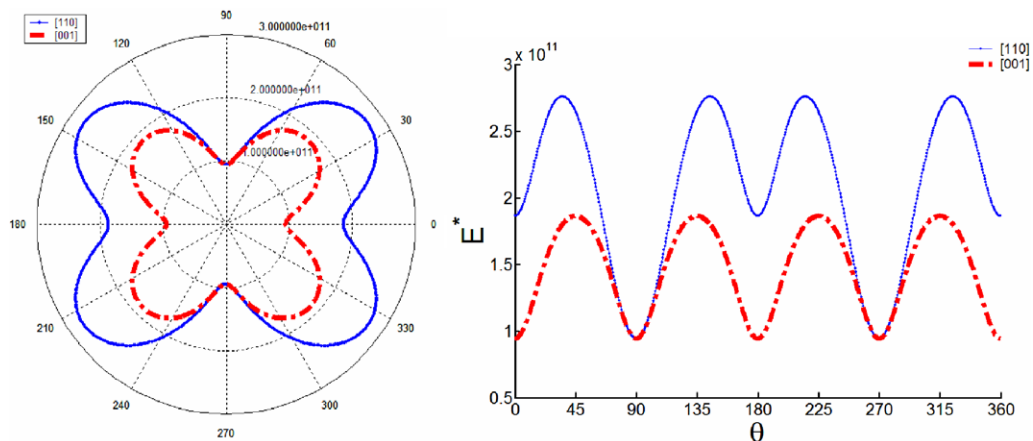

Fig. 7. Sampling spaces of E^* for [0 0 1] and [1 1 0] in plane stress, polar diagram and Cartesian representation.
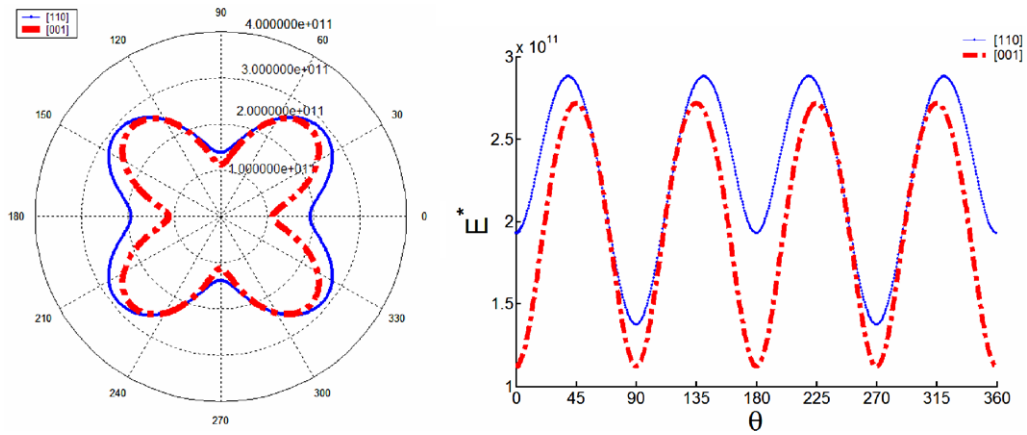
Fig. 8. Sampling spaces of E^* for [0 0 1] and [1 1 0] in plane strain, polar diagram and Cartesian representation.

Table 2
Prospect of mean values of E_{eff} and v_{eff}

	N	FEA		L1		L2	
		E (GPa)	v	E (GPa)	v	E (GPa)	v
Mean values							
Case 1	12	146.6	0.009	52.1	0.345	104.3	0.344
NiAI[0 0 1]	24	145.3	0.039	50.5	0.336	101.8	0.337
p-Stress	48	145.0	0.0S8	49.7	0.333	100.6	0.334
	96	144.3	0.059	49.4	0.332	100.0	0.333
Case 2	12	196.0	0.294	S3.6	0.344	169.0	0.342
NiAI[0 0 1]	24	194.2	0.305	81.0	0.336	164.2	0.335
p-Strain	48	193.9	0.311	79.9	0.333	162.0	0.333
	96	193.6	0.313	79.3	0.332	160.8	0.332
Case 3	12	203.4	0.238	79.8	0.336	161.1	0.336
NiAI[1 1 0]	24	202.2	0.248	77.5	0.335	156.9	0.335
p-Stress	48	201.4	0.252	76.3	0.331	154.7	0.332
	96	201.0	0.254	75.7	0.331	153.5	0.331
Case 4	12	227.5	0.276	93.7	0.340	189.5	0.338
NiAI[1 1 0]	24	226.0	0.287	91.0	0.335	184.3	0.335
p-Strain	48	225.3	0.292	89.7	0.332	181.8	0.332
	96	224.9	0.294	89.0	0.332	180.5	0.332
Case 5	12	95.6	0.280	39.3	0.342	79.4	0.340
NiAI[ISO]	24	94.9	0.289	38.1	0.335	77.2	0.334
p-Stress	48	94.6	0.294	37.6	0.333	76.2	0.333
	36	94.4	0.297	37.3	0.332	75.6	0.332

deviations σ_E and σ_v. Values are different from case to case but general trends exist. Case 1 is analyzed in detail.

Fig. 9 shows the graphs of $\langle E_{eff} \rangle$ and σ_E for Case 1 as a function of N. The asymptotic convergence of $\langle E_{eff} \rangle$ from either FEA, L1 and L2 is fast (Fig. 9A) and the estimates of $\langle E_{eff} \rangle$ from each of the three models are marginally dependent on N. The standard deviation σ_E, instead, exhibits a marked decay

and drops about one order of magnitude decay over the range of N. Invariably $\sigma_E \ll \langle E_{eff} \rangle$ for any N and for any model. For example, the standard deviation of the FEA data is less than 5% of $\langle E_{eff} \rangle$ at $N = 12$ and becomes less than 0.5% for $N = 96$. Because of the asymptotic convergence and the small scatter, the estimates for $N = 96$ are taken as asymptotic estimates for each case and model, i.e. $\langle E_{eff} \rangle_{96} \simeq \langle E_{eff} \rangle_{\infty}$. Models for $N = \{48, 96\}$ contain

Table 3
Prospect of standard deviations of E_{eff} and v_{eff}

|	N	FEA		L1		L2	
		E (GPa)	v	E (GPa)	v	E (GPa)	v
Standard deviations							
Case 1	12	7.9898	1.71E−02	1.3027	4.82E−03	2.6174	9.09E−03
NiAl[0 0 1	24	2.9532	7.61E−03	0.5015	5.22E−03	1.0027	8.63E−03
p-Stress	48	1.1335	3.79E−03	0.1883	2.60E−03	0.3779	4.57E−03
	96	0.S537	1.47E−03	0.0932	1.08E−03	0.1846	1.94E−03
Case 2	12	4.6303	2.31E−02	1.3123	7.89E−03	2.5510	5.65E−03
NiAl[0 0 1]	24	1.6851	9.39E−03	0.4997	8.28E−03	0.9771	5.31E−03
p-Strain	48	0.6550	4.12E−03	0.1865	4.16E−03	0.3739	2.76E−03
	96	0.3194	1.63E−03	0.0919	1.76E−03	0.1882	1.15E−03
Case 3	12	6.2009	1.06E−02	1.3099	3.35E−03	3.7770	7.96E−03
NiAl[1 1 0]	24	2.7456	4.80E−03	0.6928	3.80E−03	2.0058	S.84E−03
p-Stress	48	0.7910	2.89E−03	0.1885	2.48E−03	0.6029	4.66E−03
	96	0.3759	1.15E−03	0.1111	2.21E−03	0.4077	4.21E−03
Case 4	12	7.3583	1.31E−02	1.9068	7.48E−03	2.5843	4.28E−03
NiAl[1 1 0]	24	3.4959	5.92E−03	1.0247	6.40E−03	1.3556	3.44E−03
p-Strain	48	0.9777	3.93E−03	0.3004	4.38E−03	0.3784	2.66E−03
	96	0.5746	1.58E−03	0.2014	4.15E−03	0.2249	2.25E−03
Case 5	12	0.0028	1.30E−05	0.0005	4.00E−06	0.0009	4.00E−06
NiAl[ISO]	24	0.0011	6.00E−06	0.0002	4.00E−06	0.0004	4.00E−06
p-Stress	48	0.0004	3.00E−06	0.0001	2.00E−06	0.0002	2.00E−06
	96	0.0002	1.00E−06	0.0000	1.00E−06	0.0002	1.00E−06
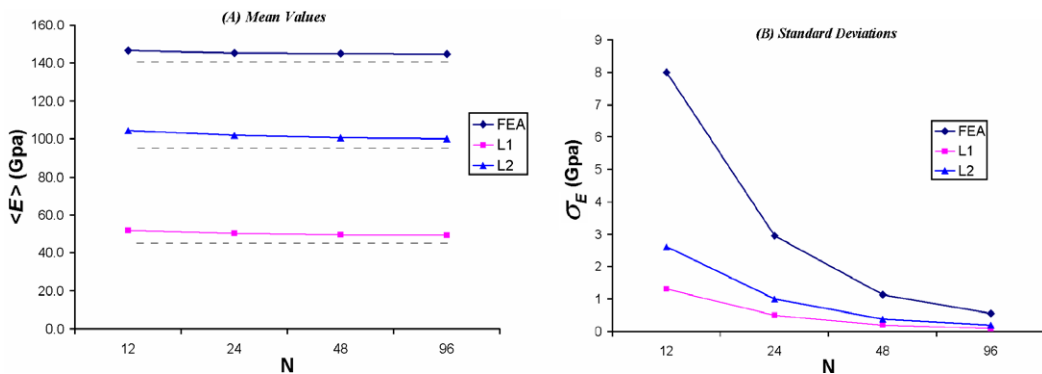
Fig. 9. Average estimates of $\langle E_{eff} \rangle$ and standard deviation σ_E as a function of N for Case 1; the asymptotic convergence of $\langle E_{eff} \rangle$ is fast (A).

more than 2000 grains and should indeed be isotropic and homogeneous on the macroscale with good approximation (Davidge, 1979).

As anticipated in Section 3.4, there is a large disproportion amongst the estimates $\langle E_{eff} \rangle$ from the three models. The FEA is much stiffer than L1 and L2, whose stiffnesses are about 33% and 70% of the FEA value, respectively. L2 is about twice as stiff as L1, reflecting the greater rigidity of the GE in comparison to an individual CST. The estimated $\langle E_{eff} \rangle$ from the plane strain cases are higher

than in the plane stress as expected. The values from $\mathbf{C}_M^{110}$ are considerably higher than the ones from $\mathbf{C}_M^{001}$, demonstrating the dependence of the estimates from 2D models on the choice of the sampling subspace. According to Miracle (1993), the value of $\langle E_{eff} \rangle$ for polycrystalline NiAl from full 3D random sampling is 199.8 GPa, which is intermediate to the FEA estimates from $\mathbf{C}_M^{001}$ and $\mathbf{C}_M^{110}$ in Table 2. The aforementioned experimental value is close to the FEA estimates from Case 2 ($\mathbf{C}_M^{001}$ in plane strain)
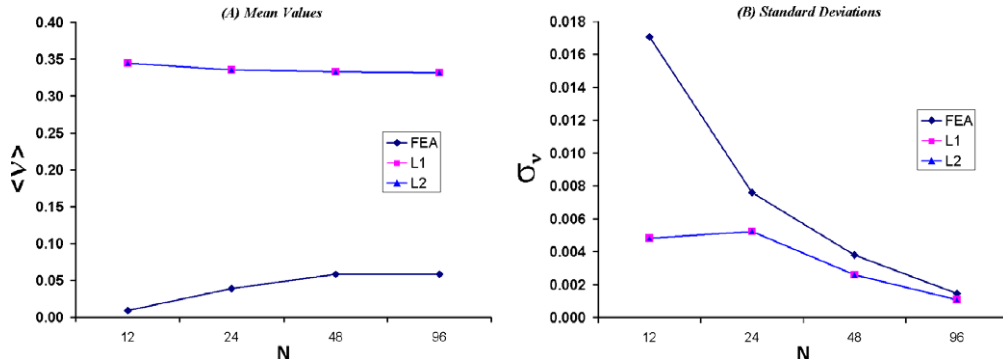
Fig. 10. Average estimates of $\langle v_{\mathrm{eff}} \rangle$ and standard deviation σ_v as a function of N for Case 1; the asymptotic convergence of $\langle v_{\mathrm{eff}} \rangle$ is fast (A). The data from L1 and L2 overlap.

and Case 3 ($\mathbf{C}_{\mathrm{M}}^{110}$ in plane stress). In comparison to L1 and L2, the FEA values of $\langle E_{\mathrm{eff}} \rangle$ are more accurate and reliable. This statement is supported by the results from the isotropic case (Case 5) where the theoretical value of the Young's modulus $E = 94.3$ GPa used in (19) is in perfect agreement with the FEA estimate $E = 94.4$ GPa.

The plots of the statistics $\langle v_{\mathrm{eff}} \rangle$ and σ_v as a function of N for Case 1 are shown in Fig. 10. The asymptotic convergence is still observed but is more evident in the two lattice models, which provide almost identical estimates. For the lattices, the Poisson ratio is mainly a function of the topology and its value settles around 0.33 for all five cases (Table 2). The asymptotic values of FEA are consistently lower than for the lattice and, instead, vary considerably from case to case, from a minimum of 0.059 (Case 1) to a maximum of 0.31 (Case 2). For Case 1 a marked mismatch is observed between the FEA and lattice, whose asymptotic estimates are 0.059 and 0.33, respectively. In the other cases, the FEA values of Poisson ratio exceed the more reasonable threshold of 0.25. Miracle reports an experimental value of $v_{\mathrm{eff}} = 0.307$, which is close to the values of Cases 2 and 4 in Table 2. A crucial information about the inaccuracy of the FEA estimates for $\langle v_{\mathrm{eff}} \rangle$ comes again from the isotropic case, where the numerical value 0.297 is significantly different from the theoretical value of $v = 0.399$ from (21). Larger models and higher-order triangular elements should improve the estimate.

We summarize and conclude from above that

- the FEA estimates of $\langle E_{\mathrm{eff}} \rangle$ are accurate and can be used as point of reference to quantify the mismatch between "true" parameters and the estimates from L1 and L2;

- the estimate $\langle v_{\mathrm{eff}} \rangle$ is a constant parameter for the lattice and it is not possible to match the value from FEA (or experiments) with these discrete lattices;
- the estimates of $\langle v_{\mathrm{eff}} \rangle$ from FEA models, unlike for $\langle E_{\mathrm{eff}} \rangle$, are not accurate and seem lower bounds of true estimates.

For Cases 1–4, mechanical disorder is introduced in the lattice by random sampling the spring stiffnesses from a quenched distribution. For Case 5, the lattices are both mechanically and geometrically perfect. Two advantages of the discretization procedures are that it is not necessary to assign the quenched distribution a priori and that they work flawlessly when there is no disorder like in Case 5. Both procedures L1 and L2 capture the non-trivial intrinsic relation between the spring constants and the random orientation of the material axes. The "Central Limit Theorem" of statistics states that the expected distribution of a random variable that depends on a primary random variable is asymptotically normal, regardless of the sampling distribution of the primary variable. Fig. 11 shows indeed that the spring constants from L1 are normally distributed. More precisely, the bulk springs and the boundary springs follow two distinct Gaussian distributions because the CST area of the boundary links is half of that in the bulk and the area is directly proportional to the CST stiffness matrix. Similarly, procedure L2 also produces two distinct distributions. However, for L1, a perfect correlation holds between the mean values of the stiffness distributions of the boundary links and of the bulk links, which are 22 GN/m^2 and 44 GN/m^2, respectively in Fig. 11. The dimension of "GN/m^2" reflects the
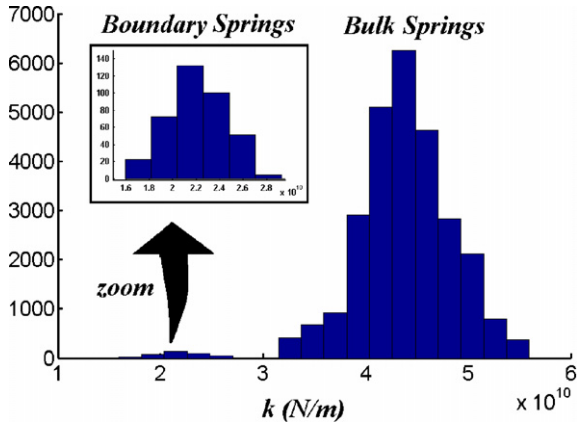
Fig. 11. Example of typical spring stiffness distribution from L1; the boundary springs and the bulk spring are sampled from two distinct Gaussian distributions.

interpretation of the spring constants as stiffness per unit thickness when the thickness is not assigned in computing $\mathbf{K}_e$. A Gaussian distribution for the stiffness has been used in the past by Mastilovic for example (Mastilovic and Krajcinovic, 1999) but this paper provides the rationale to "calculate" the natural distribution based on the geometry and mechanical property of the microstructure. Furthermore, the "Central Limit Theorem" guarantees the robustness of the results even when the sampling distribution of the material axes is not uniform. In this paper we deal only with the case of spatially uncorrelated orientations of the material axes and further research is needed to examine the case when such correlation exists.

For the isotropic Case 5, the link stiffness is not a random variable. Monette and Anderson (1994) derive the analytical formula $k = \sqrt{3}E/2$ to calculate it from the Young's modulus E. This formula returns the predicted values $k_1 = 32.3$ GPa for L1 and $k_2 = 65.5$ GPa for L2 for the respective asymptotic estimates of Young's modulus $E_1 = 37.3$ GPa and $E_2 = 75.6$ GPa. The values $\hat{k}_1 = 32.1$ GPa and $\hat{k}_2 = 64.2$ GPa measured from the numerical models are in good agreement. This provides the validation that the stiffness distribution computed by either procedure is consistent with the effective Young's modulus of the lattice.

4.3. Estimate of the correction factor

Based on the test results, the lattice models L1 and L2 can be improved to reduce the mismatch with FEA (or experimental data if available). The only free parameter of the triangular lattice is $\langle E_{\text{eff}} \rangle$, whereas $\langle v_{\text{eff}} \rangle$ is constant for all practical purposes. Within the framework of linear elasticity, the macro parameter $\langle E_{\text{eff}} \rangle$ is linearly dependent on the spring

Table 4
Prospect of corrective factors

	FEA E (GPa)	L1 E (GPa)	L2 E (GPa)	λ_1	λ_2
Case 1	144.8	49.4	100.0	2.93	1.45
Case 2	193.6	79.3	160.8	2.44	1.20
Case 3	201.0	75.7	153.5	2.66	1.31
Case 4	224.9	89.0	180.5	2.53	1.25
Case 5	94.4	37.3	75.6	2.53	1.25
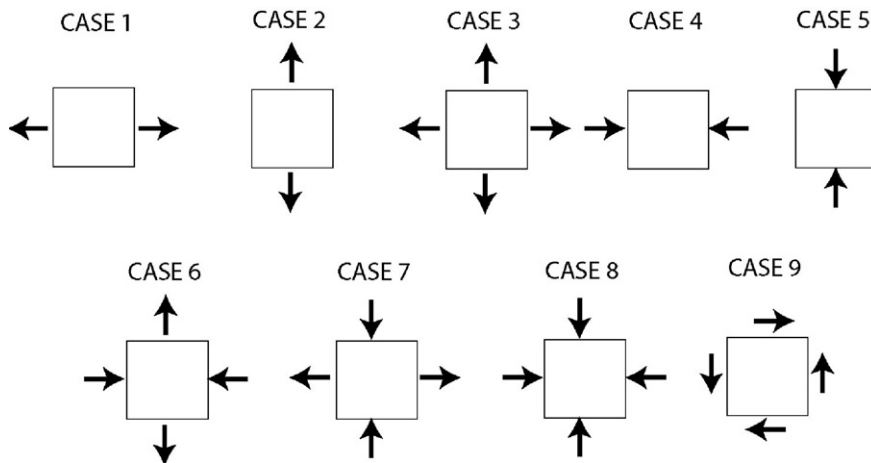
Fig. 12. Biaxial loading schemes adopted for the damage simulations.

CASE 1

CASE 2

CASE 3

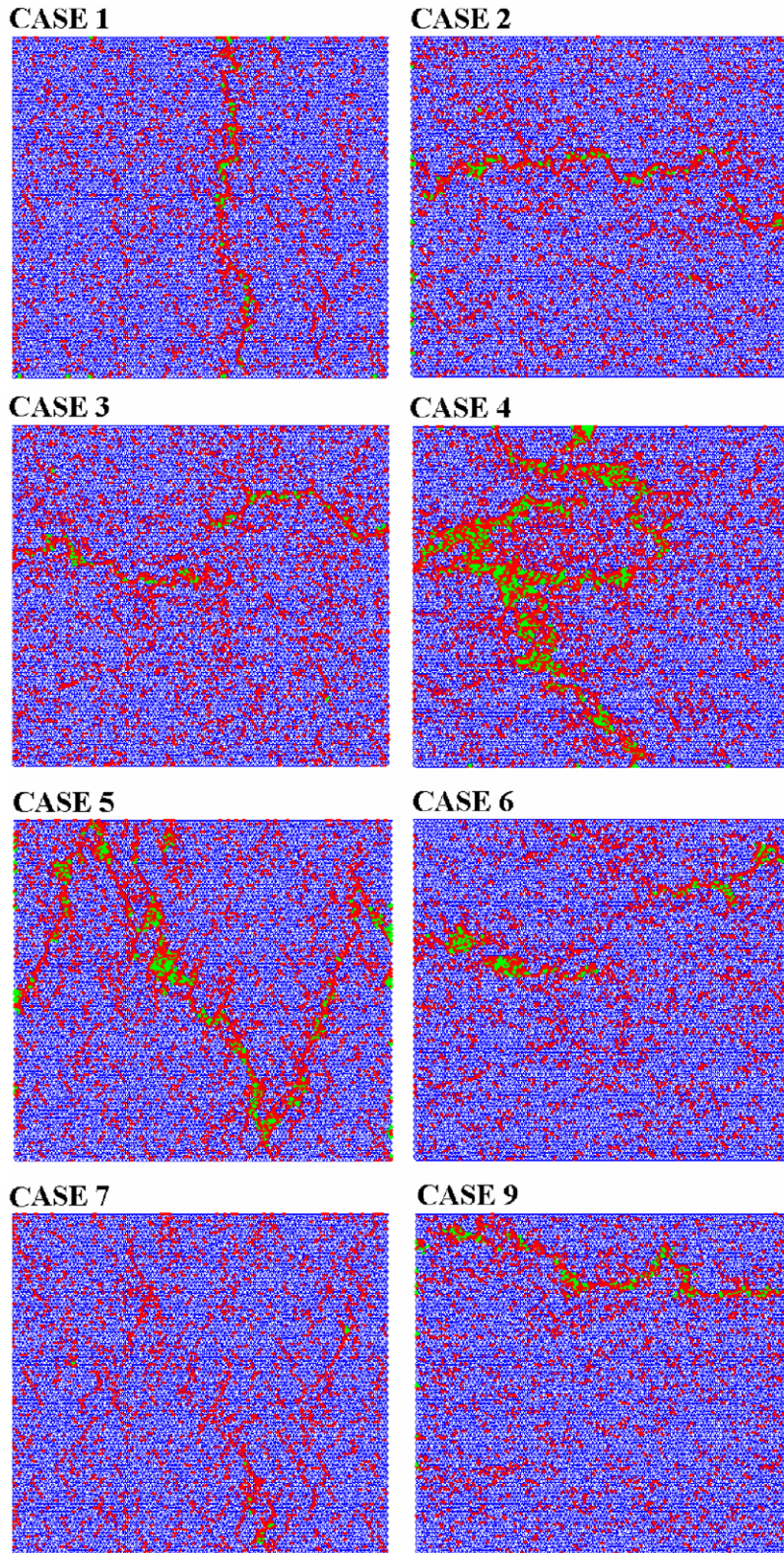CASE 4

CASE 5

CASE 6

CASE 7

CASE 9

Fig. 13. Eight failure patterns from the biaxial cases for one replicate of $N = 96$.

constant k_{ij} and for the tensile test the following identity holds:

$$U = \frac{\langle E_{\text{eff}}\rangle \bar{u}^2}{2} = \frac{1}{2}\sum_{ij}^{N_0} k_{ij}u_{ij}^2, \tag{20}$$

where U is the strain energy, $\bar{u}$ the controlled macro-displacement and u_{ij} the elongation of ijth spring. From (20), it is

$$\langle E_{\text{eff}}\rangle = \sum_{ij}^{N_0} k_{ij}\frac{u_{ij}^2}{\bar{u}^2} \tag{21}$$

and

$$\langle E_{\text{eff}}(\lambda k_{ij})\rangle = \lambda\langle E_{\text{eff}}(k_{ij})\rangle \quad \forall \lambda \in \Re, \tag{22}$$

which highlights the linear dependence. By assuming that the FEA values are good reference estimates, the lattices L1 and L2 can be calibrated on such values by scaling all the spring constants by an appropriate correction factor to match $\langle E_{\text{eff}}\rangle$. The scaling factor λ relating the target value $\langle E_{\text{eff}}\rangle^{\text{NEW}}$ to the available estimate $\langle E_{\text{eff}}\rangle^{\text{OLD}}$ is obtained from (21) and (22) as

$$\lambda = \frac{\langle E_{\text{eff}}(\lambda k_{ij})\rangle}{\langle E_{\text{eff}}(k_{ij})\rangle} = \frac{\langle E_{\text{eff}}\rangle^{\text{NEW}}}{\langle E_{\text{eff}}\rangle^{\text{OLD}}} = \frac{k_{ij}^{\text{NEW}}}{k_{ij}^{\text{OLD}}}. \tag{23}$$

While the result about the Poisson's ratio is an artifact of 2D lattice model (intrinsic mismatch from reality), the correction factor λ is not an artifact but a calibration tool providing a rational way to overcome a modeling error. In the isotropic case, Eq. (21) specializes into $k = \sqrt{3}E/2$ by Monette and Anderson which immediately provides the value $k = 81.7$ GPa corresponding to the FEA value $E = 94.4$ GPa. Hence, by virtue of (23) and based on the data in Table 2, lattice L1 and L2 would match the target E value if the spring constants were multiplied by $\lambda_1 = 94.4/37.5 = 2.53$ and $\lambda_2 = 94.4/75.6 = 1.25$, respectively. The procedure immediately extends to the other four cases as summarized in Table 4.

The correction factors depend on the lattice size but $\lambda(N) \approx$ const. for large N. The corrective factors listed in Table 4 correspond to $N = 96$, but the asymptotic convergence of $\langle E_{\text{eff}}\rangle$ allows assuming $\lambda(N = 96) \approx \lambda_\infty$.

In conclusion the steps of the discretization procedures L1 or L2 are:

1. Collection of data about the microstructure.
2. Generation a Voronoi tessellation approximating the microstructure.

3. Application of Eq. (2) in combination with (15) or (16) to generate the stiffness constants.
4. Computation of effective properties from a random sample of large lattices.
5. Obtaining reference data via experiments or finite elements.
6. Determination of corrective factor λ and lattice refinement.

More research is needed to determine which is the best model between L1 and L2. The 2D models discussed in this paper can be applied to systems where all the grains tends to have the same c-axis and the underlying assumptions are realistic, e.g. ''textured'' materials and thin polycrystalline films deposited on a substrate. In extending the methodology to the 3D case, 3D Voronoi graphs are needed and tetrahedral elements should replace the CSTs. It should be noted at this point that the 2D case is more challenging by a statistical and modeling standpoint, since it constitutes a *constrained* problem. The condition (3) disappears in 3D and all grain orientations are allowed in the microstructure. It is reasonable to expect that most of results obtained for the constrained problems in 2D would hold for the general unconstrained 3D case.

5. Application: lattice models and multiaxial damage

As mentioned in the introduction, a lattice model of a microstructure, derived and calibrated against experimental data through formulations such the ones proposed inhere, may yield quantitative results and serve a variety of purposes in the fields of solid mechanics, physics and reliability. For illustrative purposes, one can examine the case of multiaxial damage modeling, where lattice models effectively identify different types of damage localization. Damage simulations were carried out with methods analogous to Krajcinovic and Rinaldi (2005) on
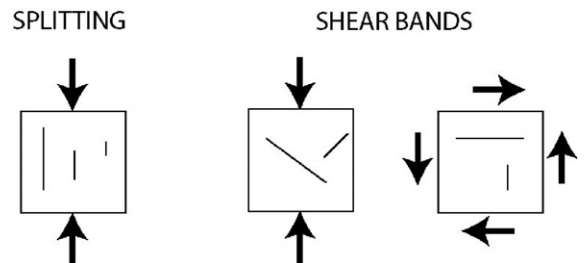
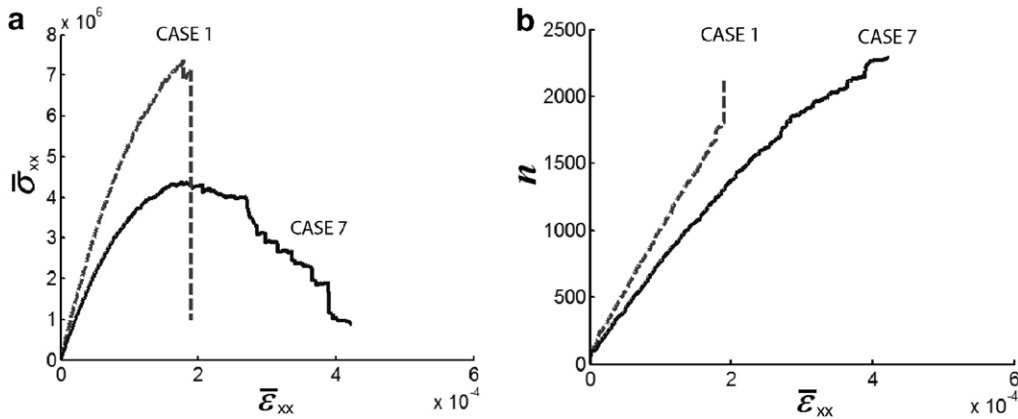

Fig. 14. Splitting and shear bands patterns.

Fig. 15. Comparison between Cases 1 and 7 for the one lattice of $N = 96$.

disordered lattices L1 for $\{001\}$ NiAl for the plane stress, i.e. using case $\mathbf{C}_M^{001}$ from (19) and $\hat{\mathbf{C}}_M^G$ from (8). This time, besides the stiffness distribution obtained from the discretization procedure, the lattices are endowed with additional disorder because both strength and length of each link are random variables sampled from arbitrarily selected uniform and Gaussian distributions, respectively. This is a manner to introduce three sources of disorder contributing to damage localization, which is more realistic. For this two-dimensional pseudo-Cauchy element with kinematic descriptors $\{\bar{\varepsilon}_{xx}, \bar{\varepsilon}_{yy}, \bar{\varepsilon}_{xy}\}$ the stress–strain space is three-dimensional. Nine biaxial loading schemes were simulated in displacement controlled load in Fig. 12, where compressive and tensile loadings in x–y directions are variously mixed in Cases 1–8 and Case 9 is pure shear. The biaxial states in cases $\{3, 6, 7, 8\}$ were run with proportional loading along x and y such that $|\bar{\varepsilon}_{xx}| = |\bar{\varepsilon}_{yy}|$. The corresponding damage patterns at the onset of failure for one lattice with $N = 96$ are shown in Fig. 13. The red[2] links are broken and the green ones are unstable links (dandling springs or mechanisms causing local instabilities and removed during the computation). Case 8 is not reported since no failure occurred for in plane hydrostatic compression. Besides the straight cracks expected for the tensile tests in Cases 1 and 2, other types of localization are observed when compressive loads are applied. Notably, mono-axial compressive tests in Cases 4 and 5, as well as pure shear in Case

9, produce either splitting and/or shear bands, schematically reported in Fig. 14. With reference to Fig. 13, splitting in Case 5 is characterized by macrocracks aligned in the direction of the applied compression, whereas shear bands are macrocracks at an angle in Cases 4 and 9. These failure modes are observed in compressive experiments on concrete, for instance in Gerstle et al. (1980), but also in lattice models from Krajcinovic and Vujosevic (1998). The existence of two failure modes when switching the compression axis between Cases 4 and 5 is intimately connected to the microstructural topology and is due to the different role of the Poisson effect in the two cases. The well known effect of lateral confinement on the ductility of the response of a brittle solid is also captured. The comparison of the macroscopic lattice responses in Fig. 15a for Cases 1 and 7 demonstrate how the lateral compression determines an increase in damage tolerance in spite of similar number of broken bonds measured at the failure (Fig. 15b). Such different stress–strain responses and localization patterns clearly reflect the peculiar development of elastic anisotropy induced by damage as a function of the loading scheme. Damage induced anisotropy has been reported by many authors (e.g. in Cordebois and Sidorff, 1979; Christopher et al., 2003). These results highlight the capability of lattice models to capture aspects not easily handled by continuum models of micromechanics. These simulations are part of a systematic study of multiaxial damage currently being conducted. Constitutive relations, statistical characterization of the response from many replicates, size effects and the detailed analysis of failure modes will be object of a next paper. In the

---

[2] For interpretation of color in Fig. 13, the reader is referred to the web version of this article.

future it seems desirable to design and carry out an experimental campaign to validate the damage simulations on calibrated lattice models.

6. Conclusions

The methodology enables to map the geometrical and mechanical properties of the real heterogeneous microstructure into a discrete spring lattice limited to the stiffness distribution of the springs. Detailed knowledge of the microstructure and a Voronoi tessellation are prerequisites. Finite elements analysis or experimental data may provide the reference for final lattice calibration. The scope of these discretization procedures exceeds the traditional techniques and includes material anisotropic and disordered geometry. The limiting case of isotropic perfect lattice from literature (Monette and Anderson, 1994) is recovered as a special case. The concept of grain element allows the creation of an intrinsic FE mesh that matches the microstructural geometry and preserves the mechanical characteristics of each grain.

While 2D spring networks can reproduce the Young's modulus of the microstructure, the results indicate that higher dimensional or more sophisticated lattices might be used to account properly for the Poisson's ratio even for plane stress and plane strain problems. However, the application of these simple 2D models seems feasible for thin textured materials.

Such lattices appear to have great potential in the study of multiaxial damage of damage-tolerant solids since they capture seamlessly the several types of localization mode observed in experiments and elastic anisotropy induced by damage. Within a modular simulation scheme, lattices might be used in synergy of micromechanics to exploit the strength of each approach.

Appendix A. Linear elasticity and Voigt notation

Within the framework of linear elasticity (Ting, 1996; Jones, 1975; Gurtin, 1975; Fung and Tong, 2001), the mechanical properties of a crystal are described by the fourth-order stiffness tensor C_{ijkl} $(i, j, k, l = 1..3)$. The symmetry conditions

$$C_{ijkl} = C_{jikl}, \quad C_{ijkl} = C_{ijlk} \quad \text{and}$$
$$C_{ijkl} = C_{klij} \tag{A.1}$$

reduce the number of independent constants from 81 to 21 for a triclinic crystal that is fully anisotropic (Ting, 1996; Jones, 1975; Gurtin, 1975; Fung and Tong, 2001). The components of the stiffness tensor are usually expressed in a local frame of reference "*a–b*" that does not coincide with the global *x–y* frame of reference as in Fig. 4. The transformation formula for C_{ijkl} in *x–y* Cartesian coordinates from the $C_{\alpha\beta\gamma\delta}$ representation in the *a–b* frame of reference is

$$C_{ijkl} = R_{i\alpha}R_{j\beta}R_{k\gamma}R_{l\delta}C_{\alpha\beta\gamma\delta}, \tag{A.2}$$

where the Einstein's convention of "repeated indices" is adopted, $\alpha, \beta, \gamma, \delta = 1..3$ and **R** is the rotation matrix. In the 2D case, where only a rotation θ around the *z*-axis is allowed, $\mathbf{R}(\theta)$ is

$$\mathbf{R}(\theta) = \begin{vmatrix} \cos\theta & \sin\theta & 0 \\ -\sin\theta & \cos\theta & 0 \\ 0 & 0 & 1 \end{vmatrix}. \tag{A.3}$$

In Fig. 3, the angle θ from *x–y* to *a–b* is positive. The sign is negative if going from *a–b* to *x–y*, such as in (a2).

Material symmetries lower the number of independent elastic constants below 21. The "symmetry group" $\mathcal{G}$, which in includes all the orthogonal tensors **R** that satisfy, defines the material symmetries

$$\mathbf{R}[\mathbf{C}\boldsymbol{\varepsilon}]\mathbf{R}^{\mathrm{T}} = \mathbf{C}[\mathbf{R}\boldsymbol{\varepsilon}\mathbf{R}^{\mathrm{T}}] \tag{A.4}$$

with $\boldsymbol{\varepsilon}$ the second-order strain tensor. Then, the grain possesses "material axes" (the axes of symmetry) related to the crystallographic orientations of the underlying Bravais lattice on the atomic scale. Orthotropic materials do not have coupling between shear strains (stresses) and normal strains (stresses) and have 9 constants in 3D and 7 constants in 2D. Rhombic, orthorhombic, cubic and isotropic materials are special cases of orthotropic materials. In Voigt notation (Jones, 1975; Gurtin, 1975) the fourth-order stiffness tensor **C** in material axes is represented by the 6×6 matrix $\mathbf{C}_{\mathrm{M}}$. For the 2D case a 4×4 matrix suffices and

$$\mathbf{C}_M = \begin{vmatrix} c_{11}^M & c_{12}^M & c_{13}^M & 0 \\ & c_{22}^M & c_{23}^M & 0 \\ & & c_{33}^M & 0 \\ symm & & & c_{66}^M \end{vmatrix}_{4\times4}$$

$$= \begin{vmatrix} c_{1111} & c_{1122} & c_{1133} & 0 \\ & c_{2222} & c_{2233} & 0 \\ & & c_{3333} & 0 \\ symm & & & c_{1212} \end{vmatrix}_{4\times4} \quad (A.5)$$

or, more conveniently in terms of the compliance matrix $\mathbf{S_M}$,

$$\mathbf{C}_M = \mathbf{S}_M^{-1} = \begin{vmatrix} \frac{1}{E_a} & -\frac{v_{ab}}{E_a} & -\frac{v_{ac}}{E_a} & 0 \\ & \frac{1}{E_b} & -\frac{v_{bc}}{E_b} & 0 \\ & & \frac{1}{E_c} & 0 \\ symm & & & \frac{1}{2G_{ab}} \end{vmatrix}_{4\times4}^{-1}, \quad (A.6)$$

where $E_a, E_b, E_c, v_{ab}, v_{ac}, v_{bc}, G_{ab}$ are the Young's moduli, the Poisson's ratios and shear Modulus measured from experiments. The material axis "c" must be parallel to the global axis z for a 2D type of problem. The matrix representation $\mathbf{C}_M^G$ of the stiffness tensor in global coordinates x–y is obtained through the matrix multiplication

$$\mathbf{C}_M^G = \mathbf{Q}(\theta)\mathbf{C}_M\mathbf{Q}^T(\theta) \quad (A.7)$$

with

$$\mathbf{Q}(\theta)$$
$$= \begin{vmatrix} \cos^2(\theta) & \sin^2(\theta) & 0 & \cos(\theta)\sin(\theta) \\ \sin^2(\theta) & \cos^2(\theta) & 0 & -\cos(\theta)\sin(\theta) \\ 0 & 0 & 1 & 0 \\ -2\cos(\theta)\sin(\theta) & 2\cos(\theta)\sin(\theta) & 0 & \cos^2(\theta)-\sin^2(\theta) \end{vmatrix}_{4\times4},$$
$$(A.8)$$

where θ is the angle from x to a and is positive as indicated in Fig. 3.

Appendix B. Energetic equivalence between CST and half-spring

The relation (15) is equivalent to the imposition of equal strain energy of the CST and the half-spring in Fig. 4. From, the work of external forces is twice the strain energy

$$W = 2U. \quad (B.1)$$

Hence we need to prove $W_{CST}^{ext} = W_{OA'}^{ext}$ or $U_{CST} = U_{OA'}$. For the CST, we have $\mathbf{du}_1 = \mathbf{du}_2 = (\cos\psi, \sin\psi)d\lambda = OA/|OA|d\lambda$ and

$$W_{CST}^{ext} = \oint_{\Gamma_1} \mathbf{F}_1 \cdot \mathbf{du}_1 + \oint_{\Gamma_2} \mathbf{F}_2 \cdot \mathbf{du}_2$$
$$= \int_0^{\lambda=1} [\mathbf{F}_1 + \mathbf{F}_2] \cdot (\cos\psi, \sin\psi)d\lambda$$
$$= \int_0^{\lambda=1} -\mathbf{F}_0 \cdot (\cos\psi, \sin\psi)d\lambda, \quad (B.2)$$

where $\mathbf{F}_1$, $\mathbf{F}_2$ are the external reactions at nodes 1 and 2 and $\mathbf{F}_1 + \mathbf{F}_2 + \mathbf{F}_0 = 0$. The dot product can be expanded from (15)

$$W_{CST}^{ext} = [-(k_{13}\cos\psi + k_{14}\sin\psi)\cos\psi$$
$$- (k_{15}\cos\psi + k_{16}\sin\psi)\sin\psi]. \quad (B.3)$$

For the OA^I half-spring we have

$$W_{OA^I}^{ext} = \int_0^{\lambda=1} F_{OA}(\lambda=1)d\lambda = \int_0^{\lambda=1} K_{OA}d\lambda = K_{OA}. \quad (B.4)$$

The equality of (B.3) and (B.4) follows from the position (15), i.e. $K_{OA} = [-(k_{13}\cos\psi + k_{14}\sin\psi)\cos\psi - (k_{15}\cos\psi + k_{16}\sin\psi)\sin\psi]$. Hence the thesis is proven.

References

Christopher, A., Mukul, K., Wayne, K.E., 2003. Analysis of grain boundary networks and their evolution during grain boundary engineering. Acta Mater. 51, 687–700.

Cordebois, J.P., Sidorff, F., 1979. Damage induced anisotropy. Colloque Euromech, 115, Villard de Lans.

Davidge, R.W., 1979. Mechanical Behavior of Ceramics. Cambridge University Press, Cambridge, UK.

Delaplace, A., Pijaudier-Cabot, G., Roux, S., 1996. Progressive damage in discrete models and consequences on continuum modelling. J. Mech. Phys. Solids 44 (1), 99–136.

Espinosa, H.D., Zavatteri, P.D., 2003. A grain level model for the study of failure initiation and evolution in polycrystalline brittle materials. Part I: theory and numerical implementation. Mech. Mater. 35, 333–364.

Fung, Y.C., Tong, P., 2001. Classical and Computational Solid Mechanics. World Scientific.

Garcia-Molina, R., Guinea, F., Luis, E., 1988. Percolation in isotropic elastic media. Phys. Rev. Lett. 60, 124–132.

Gerstle, K.H., Aschl, H., Bellotti, R., Bertacchi, P., Kotosovos, M.D., Ko, H.-Y., Linse, D., Newman, J.B., Rossi, P., Schickert, G., Taylor, M.A., Traina, L.A., Winkler, H., Zimmerman, R.M., 1980. Behavior of concrete under multiaxial stress states. J. Eng. Mech. Div. ASCE 06, 1383.

Gouyet, J.-F., 1996. Physics and Fractal Structures. Masson, Paris.

Gurtin, M.E., 1975. Truesdell, C. (Ed.), Handbuck der Physics, vol. IV.

Hansen, A., Roux, S., 2000. Statistics toolbox for damage and fracture. In: Krajcinovic, D., Mier, J.V. (Eds.), Damage and

Fracture of Disordered Materials. Springer, Wien, pp. 17–102.

Hansen, A., Roux, S., Herrmann, H.J., 1989. Rupture of central-force lattices. J. Phys. France 50, 733–744.

He, H., Thorpe, M.F., 1985. Elastic properties of glasses. Phys. Rev. Lett. 54, 2107–2110.

Jones, R.M., 1975. Mechanics of Composites Material. McGraw-Hill.

Krajcinovic, D., 1996. Damage Mechanics. North-Holland, Amsterdam, The Netherlands.

Krajcinovic, D., Basista, M., 1991. Rupture of central-force lattices. J. Phys. I 1, 241–245.

Krajcinovic, D., Rinaldi, A., 2005. Thermodynamics and statistical physics of damage processes in quasi-ductile solids. Mech. Mater. 37, 299–315.

Krajcinovic, D., Rinaldi, A., 2005. Statistical damage mechanics – 1. Theory J. Appl. Mech. (72), 76–85.

Krajcinovic, D., Vujosevic, M., 1998. Strain localization – short to long correlation length transition. Int. J. Solids Struct. 35 (31-32), 4147–4166.

Kreher, W., Pompe, W., 1989. Internal Stress in Heterogeneous Solids. Akademie Verlag, Berlin.

Mastilovic, S., Krajcinovic, D., 1999. Statistical models of brittle deformation. Part II: computer simulations. Int. J. Plast. 15, 427–456.

Miracle, D.B., 1993. The physical and mechanical properties of NiAl. Acta Metall. Mater. 41 (3), 649–684.

Monette, L., Anderson, M.P., 1994. Elastic and fracture properties of the two-dimensional triangular and square lattices. Modell. Simul. Mater. Sci. Eng. 2, 53–66.

Okabe, A., Boots, B., Sugihara, K., Chiu, S.N., 1999. Spatial Tessellations: Concepts and Applications of Voronoi Diagrams. John Wiley & Sons, New York, NY.

Sahimi, M., 2000. Heterogeneous Material II. Springer, Hew York, USA.

Schlangen, E., Van Mier, J.G.M., 1991. Experimental and numerical analysis of micromechanics of fracture of concrete. Int. J. Damage Mech. 1, 435–454.

Ting, T.C., 1996. Anisotropic Elasticity: Theory and Applications. Oxford Engineering Science Series, N 45. Oxford University Press.

Zallen, R., 1983. The Physics of Amorphous Solids. John Wiley & Sons, New York, NY.